ChemSusChem

Research Article
doi.org/10.1002/cssc.202300115

Chemistry Europe
European Chemical Societies Publishing

www.chemsuschem.org

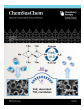

2D FeS_x Nanosheets by Atomic Layer Deposition: Electrocatalytic Properties for the Hydrogen Evolution Reaction

Raul Zazpe,*[a, b] Jhonatan Rodriguez Pereira,[a, b] Sitaramanjaneya M. Thalluri,[a, b] Ludek Hromadko,[a, b] David Pavliňák,[b] Eva Kolíbalová,[b] Michal Kurka,[a] Hanna Sopha,[a, b] and Jan M. Macak[a, b]

2-dimensional FeS_x nanosheets of different sizes are synthesized by applying different numbers of atomic layer deposition (ALD) cycles on TiO_2 nanotube layers and graphite sheets as supporting materials and used as an electrocatalyst for the hydrogen evolution reaction (HER). The electrochemical results confirm electrocatalytic activity in alkaline media with outstanding long-term stability (>65 h) and enhanced catalytic activity, reflected by a notable drop in the initial HER overpotential value (up to 26%). By using a range of characterization techniques, the origin of the enhanced catalytic activity was found to be caused by the synergistic interplay between in situ morphological and compositional changes in the 2D FeS_x nanosheets during HER. Under the application of a cathodic potential in alkaline media, the as-synthesized 2D FeS_x nanosheets transformed into iron oxyhydroxide-iron oxysulfide core-shell nanoparticles, which exhibited a higher active catalytic surface and newly created Fe-based HER catalytic sites.

Introduction

The environmental issues stemming from the use of fossil fuels, along with the ever-increasing global energy consumption, have triggered an intense search for sustainable and clean energy alternatives. Hydrogen (H_2), with one of the highest energy density values and high energy conversion efficiency, has been identified as an alternative energy source. Although total H_2 production using low emission procedures grew by 9% in 2021, nowadays most H_2 production methods are based on non-renewable sources, namely natural gas, oil reforming, and coal gasification.[1] Water is the most sustainable and renewable source of H_2. Electrochemical water splitting, in particular, based on the use of electricity to split water into H_2 and O_2 gas, represents a promising process for producing H_2 fuel.[2] Water electrolysis conducted in alkaline media is a well-established industrial technology that provides a higher stability of electrode materials than in acidic media.[3,4] However, the hydrogen evolution reaction (HER) faces several drawbacks, including sluggish kinetics and the regular use of scarce and costly noble metals as an electrocatalyst. The former is caused by the low concentration of protons under alkaline conditions, requiring further efforts to produce protons by dissociation of water near or on the catalyst surface.[2] The latter has stimulated an intense search for novel and cost-effective catalysts, based on abundant and affordable elements of the earth to replace noble metals. HER, as one of the critical steps of the water splitting process, has drawn considerable attention, with a view to developing strategies to attenuate the main drawbacks of HER that hamper the expansion of water splitting technology.[5] On the one hand, the approach of rationally designed heterostructures represents a pathway to speed up the kinetics of the HER process by generating a greater number of different active catalytic sites to assist in the cleavage of O–OH bonds.[6] On the other hand, the search for novel and cost-effective catalysts drove exploration of a wide range of materials fulfilling the aforementioned features, such as transition metal phosphides, carbides, nitrides and sulfides, among others.[7] In the case of 2-dimensional transition metal dichalcogenides (2D TMDC) and inspired by the first experimental evidence reported on the catalytic activity of MoS_2 edge sites,[8] intense research work has been devoted to exploring the catalytic properties of other 2D TMDCs, for example WS_2, $MoSe_2$, and $MoTe_2$.[9–14] 2D materials offer unique structural, optical and electronic properties as compared to the bulk counterparts. In addition, they show significant prospects as catalysts mainly due to flake-like morphology with minimal thickness, high surface-to-volume ratio, and ability to surface functionalize and adjust the catalytically active edges sites.[15,16] Among the TMDCs materials, the catalytic properties of the different phases of iron sulfide,

[a] Dr. R. Zazpe, J. Rodriguez Pereira, Dr. S. M. Thalluri, L. Hromadko, M. Kurka, Dr. H. Sopha, Dr. J. M. Macak
Center of Materials and Nanotechnologies, Faculty of Chemical Technology University of Pardubice, Nam. Cs. Legii 565, 530 02 Pardubice (Czech Republic)
E-mail: raul.zazpe@upce.cz
[b] Dr. R. Zazpe, J. Rodriguez Pereira, Dr. S. M. Thalluri, L. Hromadko, Dr. D. Pavliňák, Dr. E. Kolíbalová, Dr. H. Sopha, Dr. J. M. Macak
Central European Institute of Technology
Brno University of Technology, Purkynova 123, 612 00 Brno (Czech Republic)

Supporting information for this article is available on the WWW under https://doi.org/10.1002/cssc.202300115

namely FeS_2, Fe_3S_4 and FeS, have been largely overlooked and barely explored compared to other TMDCs, despite the relative low cost and toxicity and the high natural abundance of iron and sulfur. Previous works have reported the synthesis of mesoporous and nanostructures of FeS_2 and FeS_x employing various methods, such as, hydrothermal,[17] solvothermal,[18–26] hot injection,[27] gas phase sulfidation[28,29] and chemical vapor deposition,[30,31] and explored their electrocatalytic properties toward HER showing encouraging catalytic results.[18–22,27,28] Therein, various supporting active materials have been reported decorated with different phases of FeS_x to fabricate composites with synergistic effects. For example, FeS nanosheets were deposited on a metal foam substrate[17,18,32] and carbon fiber cloth,[26] while FeS_2 nanoparticles decorated C nanoparticles[20] and graphite oxide.[25,33] In parallel, FeS_2 decorated TiO_2 nanoparticles and TiO_2 nanotubes heterostructures were used to assess FeS_2 photoelectrochemical properties.[23,24] Although these works reported successful synthesis of various iron sulfide phases using different methods mentioned above, they require high temperatures, the use of harmful chemicals and/or are time consuming. This work approaches the synthesis of FeS_x by means of atomic layer deposition (ALD) and is essentially motivated by its unparalleled control over the thickness and chemical composition of the deposited material. ALD is a well-established deposition technique based on alternating self-limiting gas-surface chemical reactions. The precursors are introduced separately to react with the active surface sites followed by purging steps using an inert gas (N_2 or Ar) avoiding any chemical reaction in the gas phase between the precursors. The unparalleled sub-nanometer thickness control lies in the self-limiting nature of the chemical surface reactions, caused by the limited number of active surface sites (available to react with the gas phase precursor), restricting the growth process to one layer per cycle. The ALD cycle is repeated until the desired sheet thickness is achieved. More importantly, ALD is the only deposition method that enables conformal and uniform deposition on complex substrates including high aspect ratio structures and nanostructured porous materials. Furthermore, in recent years ALD has been successfully exploited for the synthesis of 2D materials of different chemical nature.[34,35] There have been few reports on the use of ALD for the synthesis of iron sulfide. Shao et al. reported the catalytic properties of ALD FeS_x coatings on porous-Al_2O_3 powder toward the hydrogenation of azo compounds; Xiong et al. presented the catalytic activity of $Fe_xCo_{1-x}S_y$ for HER; while Guo et al. published the synthesis of various metal pyrites by ALD including FeS_2.[36–38]

To our knowledge, this work is the first one to report on the electrocatalytic properties toward HER of 2D FeS_x nanosheets synthesized by applying different numbers of ALD cycles. FeS_x synthesis was carried out in a fast and simple fashion that offers significant practical advantages (low temperature, non-time consuming and single step process) applying different numbers of ALD cycles, namely 20, 60, 180 and 300, on substrates of different nature, including soda lime glass, Si wafer, annealed Ti foil, 5 μm-thick TiO_2 nanotube (TNT) layers and graphite sheets (GS). The electrocatalytic activity evaluation of FeS_x was conducted using TNT layers and GS. The choice of such supporting materials is based on the benefits obtained, as described below: TNT layers offer a unique tubular architecture, enhanced charge transfer, chemical stability, and high surface-area ratio, while GS provide high electrical charge transfer and chemical stability. Extensive physical and chemical characterization of FeS_x, carried out before and after the HER process, showed that the as-deposited FeS_x grew as 2D nanosheets randomly oriented on the surface of the substrates, and revealed the chemical composition of the as-deposited FeS_x as a mixture of iron sulfide phases, namely Fe_3S_4 (Greigite) and FeS. The electrochemical characterization confirmed the electrocatalytic activity of FeS_x toward HER. During the electrochemical HER process, the as-deposited 2D FeS_x nanosheets underwent both a chemical and a morphological transformation and turned into a core-shell structure of iron oxyhydroxide-iron oxysulfide nanoparticle aggregates, which demonstrated catalytic activity and long-term chemical stability during chronoamperometric measurements up to 65 h.

Results and Discussion

The growth of FeS_x by ALD was evaluated on substrates of different nature such as soda lime glass, Si wafer, annealed Ti foil, 5 μm-thick TNT layers and GS (chemically treated for surface activation as described in the Experimental Section). Figure 1 shows the FeS_x as-deposited on the TNT layers and GS after applying 20, 60, 180 and 300 ALD cycles. Upon applying 20 and 60 ALD cycles, discrete FeS_x nanosheets can be observed by SEM on GS surface decorated, while on TNT layers they could not be visualized given their small size. On the contrary, as the number of ALD cycles increased up to 180 and 300, the 2D FeS_x nanosheets covered extensively the surface of the GS and TNT layers, exhibiting a dominant out-of-plane orientation.

SEM top-view images (see the Supporting Information, Figure S1) also verified the growth of FeS_x on Si wafer, annealed Ti foil, and soda lime glass as a 2D flaky nanosheet structure, randomly oriented on the substrate surface. To gain a deeper understanding of FeS_x growth, it was characterized as a function of different numbers of ALD cycles (25, 50, 200, 500, 800 and 1000; Figure S2a–f). Therein, SEM top-view images show, how the initial discrete FeS_x nucleation sites observed at a low number of ALD cycles (25 and 50) turned into thin 2D flaky nanosheets with a large lateral size at a higher number of ALD cycles. The SEM cross-sectional image (Figure S2g) allowed for a rough estimation (due to uneven growth of nanosheets) of the FeS_x thin film thickness in approximately 40 nm upon 1000 cycles, while HR-TEM images illustrated the layered structure of the FeS_x nanosheets with an interlayer distance of about 5 Å (Figure S2h), which matches well with the typical FeS interlayer distance.[39] The thickness of the FeS_x nanosheets was statistically evaluated from SEM images to be 10.5 ± 1.2 nm, 11.8 ± 1.3 nm, 15.1 ± 1.6 nm and 15.9 ± 1.7 nm upon 200, 500, 800 and 1000 ALD cycles, respectively. It indicates a higher growth rate of the nanosheets on the flake edges compared to that of the basal planes, which are comparably inert.

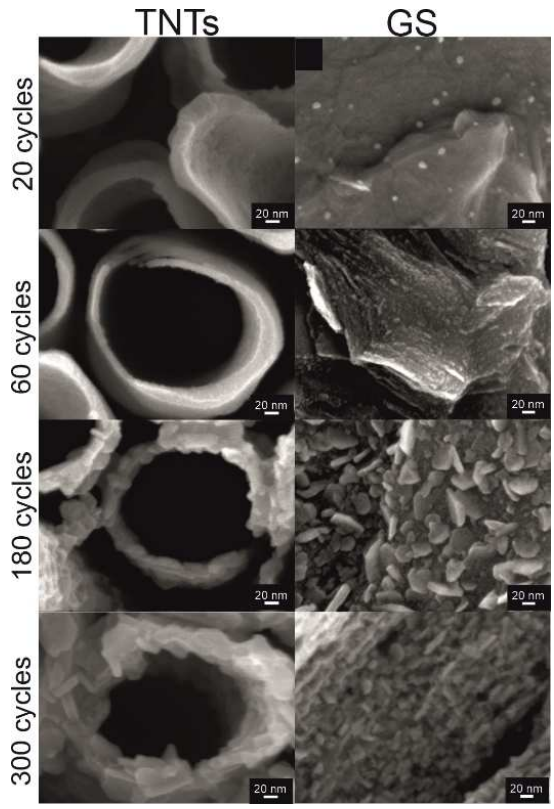

Figure 1. SEM top-view images of the 5 μm-thick TiO_2 nanotube layers (TNTs; left) and graphite sheet (GS; right) decorated with FeS_x nanosheets grown by ALD using different numbers of cycles.

The roughness and morphology of the as-deposited FeS_x upon different numbers of cycles was further characterized by atomic force microscopy (AFM; Figure S3). The AFM measurements indicated that the growth of 2D FeS_x nanosheets with random orientation increased the root-mean-square roughness (R_q; see Table S1) which is in line with the SEM observation.

Fourier Transform Infrared (DR-FTIR) spectroscopy analysis was conducted to identify surface functional groups and determine the bonding of as-deposited FeS_x. The spectrum obtained (Figure S4) showed peaks at 550 and 808 cm^{-1}. The peak at 550 cm^{-1} was ascribed to the bending vibration of sulfide groups,[40,41] while the peak at 808 cm^{-1} was associated to Fe–O–H bending vibrations.[42,43] The 1250–900 cm^{-1} region suggested the presence of products of iron oxidation and sulfur oxidation revealing that a FeS_x surface was oxidized after being exposed to air.

Grazing-incident X-ray diffractometry (GI-XRD) revealed the polycrystalline nature of the as-deposited FeS_x (Figure S5) and indicated the presence of two phases of iron sulfide, namely Fe_3S_4 (Greigite) and FeS (hexagonal). The relatively low intensity of the diffraction peaks is ascribed to the small size of the different crystallites, which are restricted by the nanoscale size of the 2D nanosheets. The diffraction peaks in the GI-XRD pattern (Figure S5) at $2\theta \approx 15°$, 29.9°, 52.5°, and 54.9° matched well with the planes (111), (113), (004) and (135) of the Fe_3S_4 phase, respectively. Regarding the peaks at $2\theta \approx 34°$ 44°, and 53.1°, they were assigned to the planes (112), (114), and (030) of the FeS (hexagonal) phase.

The FeS_x nanosheets were characterized by X-ray photoelectron spectroscopy (XPS; Figure 2). The surface chemical composition of the as-deposited FeS_x using 300 ALD cycles is shown for TNT layers (Figure 2, top row) and GS (Figure 2, botom row). In the corresponding survey spectra (Figure 2a,d), the absence/minor content of other chemical species confirms the high quality of the FeS_x deposited on both the TNT layers

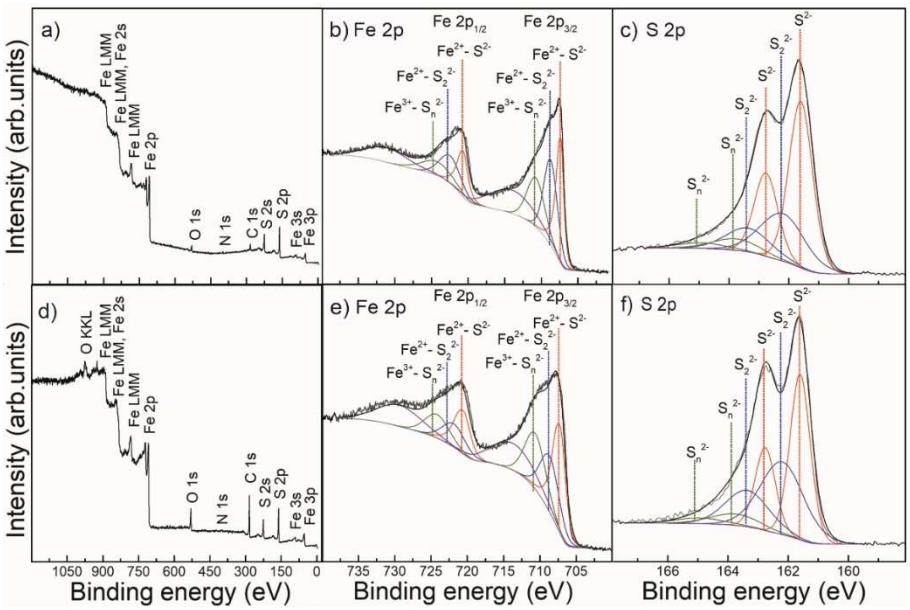

Figure 2. XPS results for as-deposited TiO_2 nanotube layers (TNT layers; left column) and graphite sheet (GS; right column) FeS_x decorated using 300 ALD cycles: (a,d) XPS survey spectra; high-resolution deconvoluted XPS spectra of (b,e) Fe2p and (c,f) S2p.

and the GS. Therefore, whereas TNT layers showed a minor content of C and O, the higher content of these elements in GS was directly related in the case of C to the nature of the substrate, and in the case of O to the generation of O-containing groups after the chemical activation process of GS (Figure S6). The high-resolution Fe2p XPS spectra (Figure 2b,e) exhibited two peaks that correspond to the spin-orbit splitting of $Fe2p_{3/2}$ and $Fe2p_{1/2}$. The corresponding deconvolution allowed us to obtain a valuable insight into the chemical composition of the as-deposited FeS_x. Thus, it was revealed that Fe displayed a mixture of oxidation states +2 and +3: (i) Fe^{2+}–S^{2-} bond at binding energies (BE) of approximately 707.3 and 720.5 eV,[44] (ii) Fe^{2+}–S_2^{2-} bond at BE of approximately 708.7 and 722.6 eV,[45] and (iii) Fe^{3+}–S_n^{2-} bond at BE of approximately 710.7 and 724.2 eV.[46]

The deconvolution of the high-resolution S2p XPS spectra (Figure 2c,f) verified these results showing a set of peaks corresponding to different sulfur species (i) monosulfide S^{2-}–Fe bond at BE values of approximately 161.6 and 162.8 eV,[44] (ii) disulfide S_2^{2-}–Fe bond at BE values of approximately 162.2 and 163.4 eV,[47,48] and (iii) polysulfide S_n^{2-}–Fe bond with BE values of approximately 163.8 and 164.9 eV.[44,48] These results suggested that the as-deposited FeS_x on both supporting materials is a high-quality material (absence of other species) composed of various iron sulfide phases, which is fully consistent with the XRD results that indicated the concomitant presence of Fe_3S_4 (Greigite) and FeS (hexagonal; troilite) phases.

The as-deposited FeS_x was further characterized by means of Raman spectroscopy at ambient conditions using both visible (532 nm) and infrared (633 nm) laser excitation wavelengths (Figure S7). It should be noted that during preliminary experiments FeS_x was found unstable when in the air for a long time, and the action of the laser on the sample induced oxidation processes generating FeOOH or Fe_2O_3 compounds. Therefore, during the main measurements, the laser power was attenuated to 6 W (532 nm) and 4 W (633 nm) with an increase in exposure time and accumulation of spectra. Raman spectra at 532 nm and 633 nm showed peaks at around 335 and 370 cm^{-1} that have been reported as characteristic bands of pyrrhotite ($Fe_{1-x}S$, where $x=0$ to 0.2).[49] Likewise, Raman spectra of troilite (FeS hexagonal) show a peak at around 335 cm^{-1} what suggests that the phases of pyrrhotite and troilite are coexisting. Fe_3S_4 was identified by the two bands at around 348 and 358 cm^{-1},[50,51] which were only visible in the spectrum obtained at 633 nm (infrared wavelength). Therefore, the Raman results confirmed that the as-deposited FeS_x is composed of Fe_3S_4, FeS (troilite) and FeS_x (where $x=0$ to 0.2), as described in the XRD and XPS results described above. Regarding the peak observed in the spectra at around 319 cm^{-1}, it could not be assigned to any Raman spectra of the iron sulfide phase. We suggest it originates by some exotic phase formed in the mixture of the phases present in the as-deposited FeS_x, since such a peak is located in the characteristic region of Fe–S bond. Moreover, Raman spectra revealed the absence of elemental sulfur (typical bands centered at 84,151, 218, 248, 437 and 474 cm^{-1}).[52]

Figure 3 shows high-resolution transmission electron microscopy (HR-TEM) images obtained on a fragment of a single TNT decorated with FeS_x using 300 ALD cycles. The high-angle annular dark-field image (Figure 3a) proved a homogeneous FeS_x decoration along the TNT wall (inner and outer surface). The area enclosed by a rectangle in Figure 3a was inspected by energy dispersive X-ray (EDX) analysis. The EDX spectra demonstrated the presence of Ti, O, Fe, and S (Figure S8a), and the elemental mapping identified a homogeneous distribution of the Ti, O, Fe, and S elements on the TNT surface without the presence of any other element confirming the chemical composition (Figure 3b–f). The chemical composition profile conducted in Figure 3b (indicated by the arrow) illustrates the sharp interface between the TNT surface and FeS_x (Figure S8b). HR-TEM images show this interface in detail and allowed to identify the TiO_2 anatase plane (101) with a characteristic

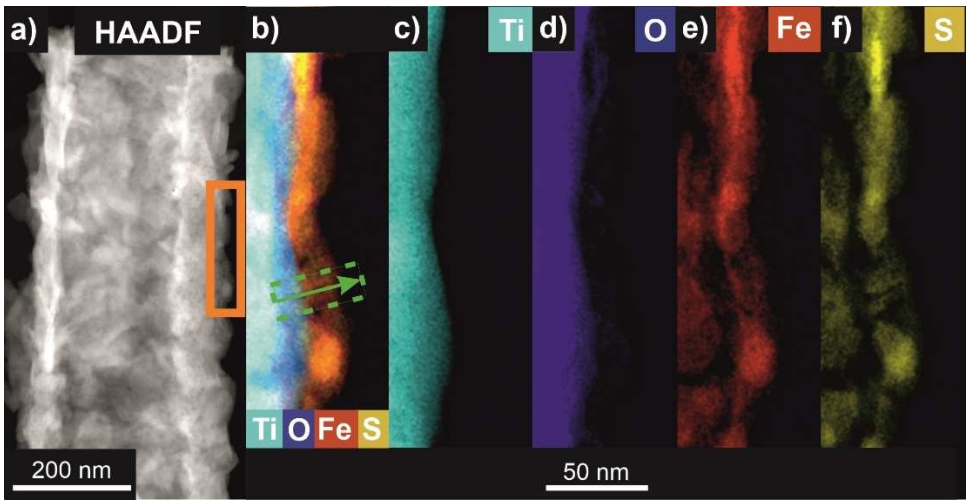

Figure 3. (a) HAADF-STEM image of a fragment of a single TNT decorated with FeS_x using 300 ALD cycles. (b) STEM EDX elemental maps of the area Ti-O–Fe–S map shown in Figure 3a, showing a color-mix overlapping of Ti-O–Fe–S maps, where the FeS_x/TNT interface and homogeneous FeS_x decoration along the TNT wall can be clearly recognized. (c–f) Corresponding STEM-EDX elemental maps that exhibit the distribution of (c) Ti, (d) O, (e) Fe, and (f) S species.

interlayer distance of about 3.5 Å and FeS_x nanosheets grown on the surface of the TNT (Figure S9).[53]

Similar results were obtained for the GS decorated with FeS_x after 180 ALD cycles. The HAADF image (Figure S10a) exhibited a GS with a set of discrete 2D FeS_x nanosheets, and the corresponding STEM EDX elemental maps (Figure S10b–f) illustrated the distribution of C, O, Fe, and S elements.

The accepted mechanism of HER in an alkaline solution involves three elementary steps [Eq. (1)–(3)]:[54]

$$\text{Volmer step}: \quad 2H_2O + e^- + * \rightarrow 2H_{ads} + 2OH^- \tag{1}$$

$$\text{Heyrovsky step}: \quad H_{ads} + H_2O + e^- \rightarrow H_2 + OH^- \tag{2}$$

$$\text{Tafel step}: \quad 2H_{ads} \rightarrow H_2 \tag{3}$$

where * denotes an active site on the catalyst surface and H_{ads} an adsorbed hydrogen atom on a catalyst active site.

The splitting of a water molecule and the subsequent adsorption of H on an active surface site is described by the Volmer step (Eq. (1)). Next, the production of H_2 proceeds by an electrochemical process (Heyrovsky step, Eq. (2)) or a chemical process (Tafel step, Eq. (3)). The HER process in an alkaline solution suffers from slow kinetics, usually two or three orders of magnitude slower than that in acidic solutions. The main reason behind this is that the first step is the dissociation of the water molecule at the active sites (the water molecule plays the role of the hydronium ion in the acidic solution).[2]

The electrocatalytic activity towards HER of FeS_x/TNT layers and FeS_x/GS composites was evaluated in 1 M KOH solution before (i.e., as-deposited FeS_x; Figures S11 and S12) and after the HER process (i.e., after chronoamperometric measurements), as shown in Figures 4 and 5, respectively. We first describe the electrocatalytic activity of as-deposited FeS_x/TNT layers (Figure S11) and FeS_x/GS composites (Figure S12) characterized by linear sweep voltammetry (LSV) applying a potential value at which all samples achieved a current density value of -10 mA cm^{-2} [-1.7 V vs Ag/AgCl (3 M); -0.664 V vs RHE], electrochemical impedance spectroscopy (EIS) and chronoamperometry (CA), using a standard three-electrode set-up (see the Experimental Section for detailed information). The HER polarization curves obtained within a potential range ($+1$ V to -0.664 V vs RHE) from the FeS_x/TNT layers (Figure S11a,b) and FeS_x/GS composites (Figure S12a,b) exhibit a marked drop in the overpotential required to reach a current density value of -10 mA cm^{-2}, as compared to the blank counterparts (Table S2), demonstrating the electrocatalytic activity towards HER. The corresponding Tafel slope values (Table S2) indicated the splitting of the water molecule and subsequent adsorption of hydrogen on a catalytic active site (Volmer reaction) as the rate-limiting step of the HER.[4] Significantly, the FeS_x/TNT layers showed lower Tafel slope values than those obtained from FeS_x/GS composites (Table S2). It was attributed to the ability of TiO_2 anatase to adsorb and dissociate water molecules, which in alkaline solution could play an important role in the reaction kinetics.[55] Thus, the splitting of water molecules was promoted in those TNT layers with a higher accessible surface of TiO_2 anatase (decorated with a lower number of FeS_x ALD cycles) speeding up the Volmer reaction kinetics (lower Tafel slope). Although in this work the FeS_x photoactivity is not explored, observation of a photoinduced semiconductor-metal transition at room temperature in ultrathin troilite FeS nanosheets was recently reported.[26] Interestingly, this phase transition revealed a superior and efficient HER catalyst, opening an exciting path to explore the photocatalytic activity of the FeS_x.

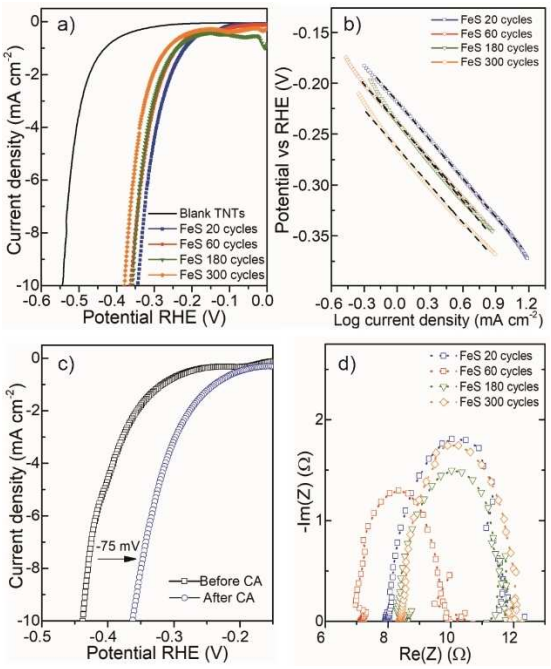

Figure 4. Electrochemical performance of TNT layers decorated with FeS_x applying different numbers of ALD cycles after the HER process: (a) HER polarization curves (iR-corrected) demonstrating electrocatalytic performance. (b) Tafel plots in 1 M KOH solution; dashed lines are provided as a guide for the eye. (c) The overpotential value required to maintain a current density of -10 mA cm^{-2} compared to the as-deposited catalyst obtained from FeS_x/TNTs decorated with 60 ALD cycles. (d) EIS measurements after the HER process.

Electrochemical impedance spectroscopy (EIS) measurements, a non-destructive and sensitive method for the evaluation of heterogenous interface properties, were conducted for investigating the heterogeneous charge transfer resistance of the FeS_x/TNT layers and FeS_x/GS composites applying a potential value [-1.5 V vs Ag/AgCl (3 M); -464 mV vs RHE]. The corresponding Nyquist plots exhibited a substantial decrease in charge transfer resistance values in those FeS_x-decorated TNT layers and GS (Table S3) compared to the blank counterparts (Figures S11c and S12c, respectively). A smaller diameter of the semicircle indicated an increased charge transfer rate (lower charge transfer resistance),[56] confirming a synergistic effect of charge transfer in composite heterostructures. Such a decrease in the charge transfer resistance was particularly prominent in the FeS_x/TNT layers.

Concerning long-term chemical stability, it was evaluated by CA measurements carried out at a potential value of -464 mV vs. RHE (Figures S11d and S12d for FeS_x/TNT layers

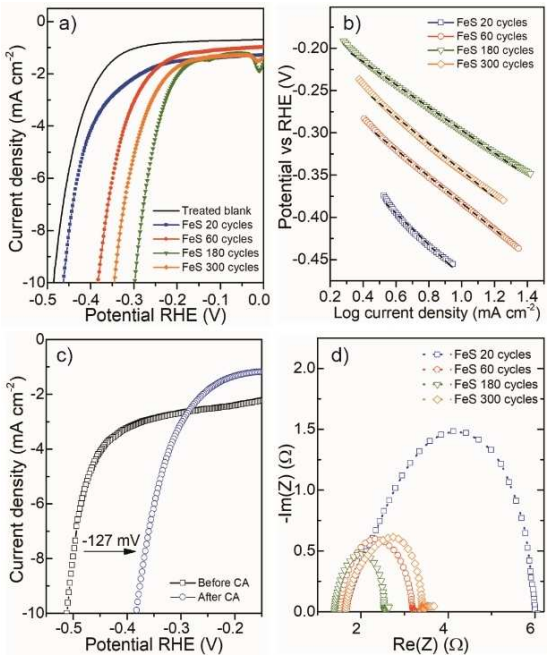

Figure 5. Electrochemical performance of GS decorated with FeS_x applying different numbers of ALD cycles after HER process: (a) HER polarization curves (iR-corrected) for GS demonstrating electrocatalytic performance. (b) Tafel plots in 1 M KOH solution; dashed lines are provided as a guide for the eye. (c) The required overpotential value needed to sustain a current density of -10 mA cm^{-2} compared to the as-deposited catalyst obtained from FeS_x/GS decorated using 60 ALD cycles. (d) EIS measurements after the HER process.

and FeS_x/GS composites, respectively). CA results revealed an outstanding catalytic activity of both composite catalysts in alkaline media. The FeS_x/TNT layers did not show degradation of the catalytic activity over time (no decrease of the current density was recorded for 16 h). Interestingly, in contrast to FeS_x/TNT layers, the FeS_x/GS composites developed a gradual and constant increase in current density to eventually reach a plateau after 45 h (Figure S12d). The cause behind this effect is described below. The chemical stability of the FeS_x/GS catalyst was further confirmed up to 68 h by long-term measurements with no degradation of catalytic activity (Figure S13).

Furthermore, the chemical stability of the catalyst under ambient conditions was also tested using a FeS_x/GS composite sample stored under ambient conditions for 60 days before conducting a second CA measurement for 25 h (application of the same conditions). Figure S14 illustrates that the catalyst exhibited very similar current density values (to those registered after 45 h of the CA test) before eventually reaching a plateau. Meaningfully, a drop up to 26% in the initial HER overpotential value required to reach 10 mA cm^{-2} (Table 1) compared to as-deposited catalyst (Table S2) was revealed by electrocatalytic activity characterization after the HER process of FeS_x/TNT layers (Figure 4a–c) and FeS_x/GS composites (Figure 5a–c).

Similarly, the EIS results showed a decrease in electron transfer resistance values (Table S3) in both FeS_x/TNT layers and FeS_x/GS composites after the HER process (Figures 4d and 5d). The electrocatalytic activity exhibited here by FeS_x/TNT layers and FeS_x/GS composites were compared to other iron sulfide materials in Table S4. However, the comparison was troublesome mainly due to significant differences in the experimental conditions applied (e.g., acidic, neutral, or alkaline media), the supporting material electrode, or the iron sulfide phase evaluated (FeS, FeS_2).

These results indicated an in-situ electrochemical catalyst activation induced during the HER process. As demonstrated by long-term stability measurements described before, the enhanced catalytic activity is irreversible, and the origin is not electronic in nature, as the HER overpotential values do not return back to its original values once the cathodic bias is removed. To discern the origin of such enhancement in catalytic efficiency, we used different characterization techniques that provided meaningful information. One reasonable approach to describe the enhanced catalytic efficiency is to determine a higher electrochemical surface area (ECSA), a key property in comparing the performance of electrocatalysts.

To test whether the higher catalytic activity (higher current density) was derived from a superior active ECSA, we estimated the corresponding electrochemical double-layer capacitance (C_{dl}) within a nonfaradaic current potential range by cyclic voltammetry (CV). This is a potential range where no Faradaic process (redox reactions) occurs, and the current is assumed to originate by capacitive charging. The proportional relation between ECSA and C_{dl} allows to relate higher C_{dl} values to greater ECSA.[57] Figures S15–S18 exhibit the CVs obtained at different scan rates (see detailed description in the Experimental section) along with the calculated double-layer capacitance obtained before and after the HER process for the FeS_x/TNT layers and FeS_x/GS composites, decorated by applying 20, 60,

Table 1. Overpotential at the cathodic current density of 10 mA cm^{-2} and Tafel slope obtained for the TNT layers and GS decorated with FeS_x using different numbers of ALD cycles in 1 M KOH solution after the HER process.

FeS_x ALD cycles	TNT samples		GS samples	
	Overpotential [mV][a]	Tafel slope [mV dec^{-1}]	Overpotential [mV][a]	Tafel slope [mV dec^{-1}]
Blank	543	167	486	355
20	343	123	463	249
60	362	123	384	191
180	357	126	311	147
300	379	117	362	185

[a] Overpotential value at the current density -10 mA cm^{-2}.

180 and 300 ALD cycles. The respective double layer capacitance values shown in Table S5 verified a significant increase in ECSA (data not shown) after the HER process for both FeS_x/TNT layers and FeS_x/GS composites compared to the ECSA of as-prepared catalysts. Importantly, subsequent SEM analysis revealed an irreversible change in the morphology of the as-deposited 2D FeS_x nanosheets into aggregates of nanoparticles distributed on the surface of both FeS_x/TNT layers and FeS_x/GS composites after the HER process (Figure S19). The presence of those nanoparticle aggregates distributed on the TNT layers and GS formed during the HER process was further confirmed by additional HR-TEM images (Figures S20 and S21). Thus, on the basis of these results, the higher ECSA obtained after the HER process was ascribed to the morphological transformation (called self-optimizing morphological changes) experienced by the initial FeS_x nanosheets to nanoparticle aggregates shape, which would exhibit a larger surface area. In fact, previous works on TaS_2 and NbS_2 suggested the beneficial impact of self-optimizing morphological changes in layered TMDCs on the electrocatalytic activity towards HER by improving charge transfer and accessibility of active sites.[58,59]

In parallel, the EDX analyses (Figures S20 and S21) confirmed the presence and consistent distribution of Fe, S, and O confined within the boundaries of the nanoparticle aggregates, while the XPS analysis provided the surface chemical composition of the nanoparticle aggregates formed (Figure S22). Survey spectra (Figures S22a,d) confirmed the absence of other chemical species, except K (from the 1 M KOH solution). The high-resolution Fe2p XPS spectra (Figures S22b,e) exhibited two peaks corresponding to spin-orbit splitting of $Fe2p_{3/2}$ and $Fe2p_{1/2}$ with BE of approximately 710.5 and 724.0 eV respectively, significantly ascribed to the presence of a Fe–O bond which suggested the replacement of S by O on the surface of the nanoparticles. The corresponding deconvolution provided more detailed information, revealing that the peaks matched well with the presence of Fe^{3+}–O bond (BE ≈ 710.5 and 724 eV),[60,61] and Fe–OH (BE ≈ 712.6 and 726.7 eV),[62,63] suggesting the formation on the nanoparticle surface of the iron oxide-hydroxide FeO(OH). XPS measurements also ruled out the origin of the enhanced catalytic activity displayed by the FeS_x/GS samples to the presence of Ag nanoparticles on the catalyst surface (diffused from the reference electrode Ag/AgCl). Interestingly, an additional peak was observed in the deconvoluted GS spectra exhibited at a BE of approximately 706.4 and 719.5 eV (not detected in TNT layers spectra), which revealed the presence of elemental iron (Fe^0).[64,65] The high-resolution XPS spectra S2p (Figure S22c,f) indicated that upon replacement of S by O, the content of S at the surface of the nanoparticles was too low (under XPS detection limits). The lack of metallic Fe^0 in the TNT layers samples is particularly interesting, as the FeS_x deposited on both supporting materials (TNTs layers and GS) can be fully comparable and all the FeS_x samples (both TNT layers and GS) have experienced identical experimental conditions. In fact, assuming the reduction of FeS_x nanosheets under the application of a proper negative potential value (in this case −0.6 V vs RHE),[18] it would denote the existence of a competing reduction reaction in the case of the TNT layers samples that hampers the reduction of Fe^{3+}/Fe^{2+} to Fe^0. Therefore, we propose that a plausible competing reduction reaction in TiO_2 under a high enough cathodic potential value is the reduction of Ti^{4+} to Ti^{3+} (by electron injection). The high-resolution Ti2p XPS deconvoluted spectra conducted in blank TNT layers before and after CA measurement for 22 h demonstrated an increase in Ti^{3+} content of almost 1% (Table S6). Therefore, we assume that the ability of Ti^{4+} to scavenge injected electrons under the proper cathodic potential value impedes the reduction of Fe^{3+}/Fe^{2+} to Fe^0 unlike in the GS samples, where the electrons effectively reduce Fe^{3+}/Fe^{2+} to Fe^0. On the basis of these findings, we attributed the enhanced electrocatalytic activity displayed by FeS_x/GS composites to the presence of Fe^0 (providing a higher electron density).

Interestingly, the XRD analysis obtained upon the HER process (Figure S23) indicated the presence of FeS and Fe_2O_3. The diffraction peak at $2\theta \approx 44°$ was assigned to the (114) crystal plane of FeS, while the diffraction peaks at $2\theta \approx 35°$ and 40° matched well with the crystal planes of hematite Fe_2O_3 (110), and (113), respectively. These XRD results were in good agreement with those provided by XPS and confirmed the content of Fe_2O_3 in the nanoparticle aggregates.

In order to describe the chemical composition changes experienced by as-deposited FeS_x nanosheets, it is essential to consider the stability of iron sulfides under negative applied potentials in alkaline media. Therefore, the conversion of iron sulfides in alkaline media into hydroxide and oxyhydroxide by replacement of sulfur with oxygen can be expected as they are not thermodynamically stable.[66–68] In parallel, the application of a negative potential (in this case −0.6 V vs RHE) leads to a partial reduction of FeS_x nanosheets that can cause the presence of metallic Fe in the core of the nanoparticles.[18] The result would be a core-shell iron oxide-hydroxide-iron oxysulfide FeO(OH) –FeO_xS_y/FeS_x structure during electrochemical reduction.

All of the above results allowed us to propose that the initial ALD deposited 2D FeS_x nanosheets underwent an irreversible morphological transformation and chemical composition change generated in situ during the HER process (i.e., under the application of certain working potential). The nature of the resulting nanoparticle aggregates is a core-shell structure in which a FeO(OH) shell enfolds an FeO_xS_y/FeS_x core (coupled with Fe^0 in GS samples). The morphological transformation into nanoparticle aggregates brings about two beneficial effects on the electrocatalytic activity: (i) a higher effective active surface area by improving accessibility of the electrolyte to the active sites enabling enhanced mass and electron transfer; (ii) shorter interlayer electron-transfer pathways that reduce the charge-transfer resistance.

In terms of the effect of the chemical composition change into FeO(OH)–FeO_xS_y on the HER catalytic activity, it is based on several factors. First, a previous work reported a study based on density functional theory (DFT) that studied the water adsorption on the surface of hematite Fe_2O_3.[69] The results revealed that dissociative molecular water adsorption on Fe^{3+} ion is more favorable than molecular adsorption. This starts the

Volmer step of the HER process in alkaline media, that is, the cleavage of the water molecule. According to the DFT results, the adsorption takes place when a single water molecule attaches with its oxygen atom to an Fe^{3+} surface ion and the water molecule forms a hydrogen bond with a neighboring surface oxygen ion. Second, the newly created Fe-based catalytic active sites with favorable free energy of H* (ΔG_{H^*}) as recently described for FeS/iron foam catalysts.[18] The authors created an S/O-covered Fe surface as a theoretical model and an O-covered Fe surface for comparative purposes to shed light on the origin of the electrocatalytic activity of these core-shell nanostructures. The authors evaluated on both surfaces the possible adsorption sites and the corresponding ΔG_{H^*}. The results showed how the S/O-covered Fe (111) surface exhibited more efficient catalytic active sites, caused by the content of S. The key point lies in the significantly different electronegativity values of S (2.58) and O (3.44). The weaker ability of S atoms to attract electrons induces a higher electron density on Fe atoms, generating effective Fe-based catalytic sites toward HER, which cannot originate on the O-covered Fe surface. Third, another factor to consider is the role of the surface hydroxy groups in enhancing the wettability of the electrode, which facilitates the transportation of molecules/ions to the catalytic active sites. In summary, the enhanced catalytic activity derived from the interplay between the newly created Fe-based catalytic active site, enhanced wettability, and a higher catalytic surface area.

Conclusion

Herein, we have presented 2-dimensional FeS_x nanosheets of different sizes as an electrocatalyst for the hydrogen evolution reaction (HER). 2D FeS_x nanosheets were synthesized by applying different numbers of atomic layer deposition (ALD) cycles on TiO_2 nanotube layers and graphite sheets as supporting materials. The synthesis was carried out in a fast and simple fashion, offering significant practical advantages as compared to other synthesis methods. The 2D FeS_x nanosheets confirmed their electrocatalytic activity, exhibiting enhanced catalytic activity performance and outstanding long-term stability in alkaline media. The synergistic interplay between in situ self-optimizing morphological and chemical composition changes during HER was revealed to be the origin of the enhanced catalytic activity. Therefore, the initial 2D FeS_x nanosheets experienced a transformation to core-shell nanoparticle aggregates with a higher catalytic surface area, while changes in the chemical composition of FeO(OH)–FeO_xS_y exhibited newly created Fe-based catalytic active sites with a favorable ΔG_{H^*}. These results confirmed the catalytic properties of Fe-based materials encouraging further works toward the development of catalysts based on earth-abundant and affordable elements.

Experimental Section

TiO_2 nanotube layers fabrication

The self-organized TiO_2 nanotube layers (TNT layers) were fabricated via electrochemical anodization of Ti foils as described in our previous works.[70] The as-prepared amorphous 5 μm-thick TNT layers turned into anatase phase after annealing in a muffle oven at 400 °C for 1 h.[71,72]

Surface activation of graphite substrates

To generate active surface sites, the surface of the commercial graphite sheets (Goodfellow, 99.95%) had to be activated. The activation method applied was mild chemical oxidation. The graphite sheets were refluxed for 5 h in HNO_3 (65%) at 110 °C, sonicated in distilled water for 5 min and dried with nitrogen prior to the ALD process.[73] This acid treatment induced the generation of functional groups (hydroxy groups) on the surface of the graphite substrates that acted as nucleation sites during the ALD process, allowing the growth of the material (FeS_x).

Atomic Layer Deposition of FeS_x

The FeS_x ALD process was carried out by applying a deposition temperature of 200 °C (Beneq-TFS 200). The growth of ALD FeS_x was evaluated on different substrates: soda lime glass, Si wafer, annealed Ti foil, 5 μm-thick TNT layers and GS. The Fe precursor was bis(*N*,*N*′-di-*t*-butylacetamidinato)iron(II) (Strem, min. 98%) while hydrogen sulfide (Messer, 99.5%) was used as the S source. The Fe precursor was heated to 90 °C to obtain a sufficiently high vapor pressure. An ALD cycle was defined by the subsequent sequence: H_2S precursor (1.25 s)-N_2 purge (14 s)-Fe precursor (1.5 s)-N_2 purge (14 s). The number of cycles applied were 20, 60, 180 and 300. N_2 (99.9999%) was used as the carrier gas at a flow rate of 500 standard cubic centimeters per minute (sccm).

Characterization techniques

The evaluation of the morphology and structure of FeS_x on the different substrates was conducted by field-emission scanning electron microscope (FE-SEM) JEOL JSM 7500F and a high-resolution transmission electron microscope (HRTEM) Thermo Fisher Scientific Titan Themis 60–300, operated at 300 kV and equipped with a C_s image aberration corrector, a high angle annular dark field detector for scanning transmission electron microscopy (HAADF-STEM) imaging, and a Super-X energy dispersive X-ray (EDX) spectrometer with four 30 mm^2 windowless detectors for STEM-EDX analysis. The dimensions of the FeS_x nanosheets were measured and statistically evaluated using proprietary Nanomeasure software.

The roughness and morphology of the FeS_x was determined in air by atomic force microscopy (AFM) using the NTEGRA (NT-MDT) system and applying tapping mode with a HA-HR tip (ScenSans) and a step of 8 nm. The roughness value was obtained as the mean value of 3 measurements of a scanned area of 2×2 μm^2.

IR spectra (resolution 2 cm^{-1}, 64 scans) were recorded on a Vertex 70v FTIR spectrometer (Bruker, Germany) using a single-bounce diamond ATR crystal.

Regarding the chemical surface composition of FeS_x, it was monitored by X-ray photoelectron spectroscopy (XPS) (ESCA2SR, Scienta-Omicron) using a monochromatic $Al_{K\alpha}$ (1486.7 eV) X-ray source operated at 250 W. The binding energy scale correction for TNT layers was carried out using the adventitious carbon C1s at

284.8 eV, while for graphite sheets the sp^2 carbon at 284.0 eV was used. Data analysis was performed with the CasaXPS program (Casa software Ltd.). Quantitative analysis was performed using the elemental sensitivity factors provided by the manufacturer.

X-ray diffraction (XRD) analysis was performed using Panalytical Empyrean with Cu tube and Pixcel3D detector. Grazing incidence X-ray diffraction was performed to obtain diffraction peaks of the as-deposited FeS_x. The incident angle was 1 degree. The patterns were recorded in the range of 5–65°, step size was 0.026 degrees, and the time per step 11 s.

Raman spectroscopy measurements were acquired under ambient conditions using the WITec confocal Raman imaging system alpha300 R equipped with 532 and 633 nm lasers. Measurements were taken by 532 nm (green) and 633 nm (red) laser excitation source in the range 100–800 cm^{-1}. To minimize a potential oxidation process of the sample, the laser power was decreased to 6 W (532 nm) and 4 W (633 nm) with an increase in exposure time (120 s for 532 nm, and 40 s for 633 nm wavelength) and accumulation of spectra (×10 for 532 nm, and ×5 for 633 nm wavelength). Savitzky-Golay process was performed to reduce the signal noise of the red laser spectrum (633 nm).

AUTOLAB (PGSTAT 204; Metrohm Autolab B. V.; Nova 1.10 software) electrochemical workstation was used to conduct the electrochemical HER measurements using a 3-electrode system. The electrocatalytic activity of the FeS_x/TNT layers and FeS_x/GS towards HER was evaluated by cyclic voltammetry (CV) in 1 M KOH in the potential range from +0.1 V to −1 V vs Ag/AgCl (3 M) using a standard three-electrode set-up with a carbon rod as counter electrode. The scan rate was 2 mV s^{-1}. The first negative scans for all FeS_x/TNT layers and FeS_x/GS are shown in the polarization curves (see the Results and Discussion section). The potentials were quoted against the reversible hydrogen electrode (RHE) using Equation (4), and the current densities were normalized to the geometric surface area (1 cm^2) of the samples exposed to the solution. Potentials were converted to the reversible hydrogen electrode (RHE) scale by using Equation (4).

$$E_{RHE=}E + (0.059\ V)pH + E^0_{ref\ vs\ SHE} \quad (4)$$

with $E^0_{ref\ vs\ SHE} = 0.210$ V, which is the standard potential of the reference electrode Ag/AgCl (3 M KCl) vs the standard hydrogen electrode (SHE) and the pH was considered 14.

Chronoamperometry (CA) was performed for the TNT layers and GS coated with 20, 60, 180 and 300 FeS_x ALD cycles in 1 M KOH at −464 mV versus RHE for 16 and 45 h, respectively.

Electrochemical impedance spectroscopy (EIS) measurements were performed in the frequency range of 10 mHz–100 kHz with an AC voltage amplitude of 10 mV applying a potential value of −464 mV vs RHE.

The electrochemically active surface area (ECSA) was estimated from the electrochemical double-layer capacitance (C_{dl}) measured in a non-Faradaic potential region, where the measured current is assumed to be due to double-layer charging. The double-layer charging current, i_c, is measured from cyclic voltammetry (CV) at different scan rates. The charging current is equal to the product of the scan rate, v, and the electrochemical double-layer capacitance, C_{dl}, as given by Equation (5):[74]

$$i_c = v \times C_{dl} \quad (5)$$

Thus, a plot of i_c as a function of v yields a straight line with a slope equal to C_{dl}.

The electrochemical capacitance was monitored by sweeping the potential from 0.74 to 0.84 V (vs RHE) and back to 0.74 V in the case of TNT layers, and from 0.89 to 0.99 V (vs RHE) and back to 0.89 V in the case of GS. Nine different scan rates were applied (20, 30, 40, 50, 60, 70, 80, 90 and 100 mV s^{-1}) were applied measuring ten CVs in each. The capacitive currents were measured as a function of the scan rate. Such potential ranges of 0.74 to 0.84 V and 0.89 to 0.99 V (vs. RHE) were selected because no apparent electrochemical features corresponding to the faradic current were observed. The linear dependence found between the current and the scan rate is consistent with the capacitive charging behavior. In the case of faradaic process, a square root dependence with respect to the scan rate would be observed due to mass transfer limitations (diffusion processes).

Acknowledgements

The authors acknowledge the Ministry of Education, Youth and Sports of the Czech Republic (MEYS CR, project LM 2018103, LM2023037) and CzechNanoLab Research Infrastructure supported by MEYS CR (LM2018110) for the financial support of the measurements/sample fabrication at CEITEC Nano Research Infrastructure. The authors also thank Jan Michalicka for TEM analysis, and Dr. Zuzana Frumarova for FTIR measurements.

Conflict of Interests

The authors declare no conflict of interest.

Data Availability Statement

The data that support the findings of this study are available in the supplementary material of this article.

Keywords: atomic layer deposition · electrocatalysis · hydrogen evolution reaction · iron sulfide · thin films

[1] International Energy Agency, "IEA (2022), Hydrogen, IEA, Paris, http://www.iea.org/reports/hydrogen," **2022**.
[2] Z. P. Ifkovits, J. M. Evans, M. C. Meier, K. M. Papadantonakis, N. S. Lewis, *Energy Environ. Sci.* **2021**, *14*, 4740–4759.
[3] X. Liu, R. Guo, K. Ni, F. Xia, C. Niu, B. Wen, J. Meng, P. Wu, J. Wu, X. Wu, L. Mai, *Adv. Mater.* **2020**, *32*, 2001136.
[4] N. Mahmood, Y. Yao, J.-W. Zhang, L. Pan, X. Zhang, J.-J. Zou, *Adv. Sci.* **2018**, *5*, 1700464.
[5] S. A. Grigoriev, V. N. Fateev, D. G. Bessarabov, P. Millet, *Int. J. Hydrogen Energy* **2020**, *45*, 26036–26058.
[6] J. Wei, M. Zhou, A. Long, Y. Xue, H. Liao, C. Wei, Z. J. Xu, *Nano-Micro Lett.* **2018**, *10*, 75.
[7] P. Yu, F. Wang, T. A. Shifa, X. Zhan, X. Lou, F. Xia, J. He, *Nano Energy* **2019**, *58*, 244–276.
[8] T. F. Jaramillo, K. P. Jørgensen, J. Bonde, J. H. Nielsen, S. Horch, I. Chorkendorff, *Science* **2007**, *317*, 100–102.
[9] J. Bonde, P. G. Moses, T. F. Jaramillo, J. K. Nørskov, I. Chorkendorff, *Faraday Discuss.* **2009**, *140*, 219–231.
[10] M. Jiang, J. Zhang, M. Wu, W. Jian, H. Xue, T. W. Ng, C. S. Lee, J. Xu, *J. Mater. Chem. A* **2016**, *4*, 14949–14953.
[11] J. C. McGlynn, T. Dankwort, L. Kienle, N. A. G. Bandeira, J. P. Fraser, E. K. Gibson, I. Cascallana-Matías, K. Kamarás, M. D. Symes, H. N. Miras, A. Y. Ganin, *Nat. Commun.* **2019**, *10*, 4916.

[12] M. Motola, M. Baudys, R. Zazpe, M. Krbal, J. Michalička, J. Rodriguez-Pereira, D. Pavliňák, J. Přikryl, L. Hromádko, H. Sopha, J. Krýsa, J. M. Macak, *Nanoscale* **2019**, *11*, 23126–23131.
[13] R. Zazpe, H. Sopha, J. Charvot, R. Krumpolec, J. Rodriguez-Pereira, J. Michalička, J. Mistrík, D. Bača, M. Motola, F. Bureš, J. M. Macak, *Appl. Mater. Today* **2021**, *23*, 101017.
[14] L. Zheng, F. Teng, X. Ye, H. Zheng, X. Fang, *Adv. Energy Mater.* **2020**, *10*, 1902355.
[15] S. H. Noh, J. Hwang, J. Kang, M. H. Seo, D. Choi, B. Han, *J. Mater. Chem. A* **2018**, *6*, 20005–20014.
[16] D. Voiry, J. Yang, M. Chhowalla, *Adv. Mater.* **2016**, *28*, 6197–6206.
[17] Z. Pan, M. Yaseen, P. Kang Shen, Y. Zhan, *J. Colloid Interface Sci.* **2022**, *616*, 422–432.
[18] X. Zou, Y. Wu, Y. Liu, D. Liu, W. Li, L. Gu, H. Liu, P. Wang, L. Sun, Y. Zhang, *Chem* **2018**, *4*, 1139–1152.
[19] C. Di Giovanni, W. A. Wang, S. Nowak, J. M. Grenèche, H. Lecoq, L. Mouton, M. Giraud, C. Tard, *ACS Catal.* **2014**, *4*, 681–687.
[20] Z. Li, M. Xiao, Y. Zhou, D. Zhang, H. Wang, X. Liu, D. Wang, W. Wang, *Dalton Trans.* **2018**, *47*, 14917–14923.
[21] M. Villalba, J. Peron, M. Giraud, C. Tard, *Electrochem. Commun.* **2018**, *91*, 10–14.
[22] C. Di Giovanni, Á. Reyes-Carmona, A. Coursier, S. Nowak, J. M. Grenèche, H. Lecoq, L. Mouton, J. Rozière, D. Jones, J. Peron, M. Giraud, C. Tard, *ACS Catal.* **2016**, *6*, 2626–2631.
[23] T. R. Kuo, H. J. Liao, Y. T. Chen, C. Y. Wei, C. C. Chang, Y. C. Chen, Y. H. Chang, J. C. Lin, Y. C. Lee, C. Y. Wen, S.-S. Li, K.-H. Lin, D.-Y. Wang, *Green Chem.* **2018**, *20*, 1640–1647.
[24] Y. Xin, Z. Li, W. Wu, B. Fu, Z. Zhang, *ACS Sustainable Chem. Eng.* **2016**, *4*, 6659–6667.
[25] J. Jiang, L. Zhu, H. Chen, Y. Sun, W. Qian, H. Lin, S. Han, *J. Mater. Sci.* **2019**, *54*, 1422–1433.
[26] G. Zhou, Y. Shan, L. Wang, Y. Hu, J. Guo, F. Hu, J. Shen, Y. Gu, J. Cui, L. Liu, X. Wu, *Nat. Commun.* **2019**, *10*, 399.
[27] D. Jasion, J. M. Barforoush, Q. Qiao, Y. Zhu, S. Ren, K. C. Leonard, *ACS Catal.* **2015**, *5*, 6653–6657.
[28] R. Miao, B. Dutta, S. Sahoo, J. He, W. Zhong, S. A. Cetegen, T. Jiang, S. P. Alpay, S. L. Suib, *J. Am. Chem. Soc.* **2017**, *139*, 13604–13607.
[29] D. R. Cummins, H. B. Russell, J. B. Jasinski, M. Menon, M. K. Sunkara, *Nano Lett.* **2013**, *13*, 2423–2430.
[30] L. Samad, M. Cabán-Acevedo, M. J. Shearer, K. Park, R. J. Hamers, S. Jin, *Chem. Mater.* **2015**, *27*, 3108–3114.
[31] N. Berry, M. Cheng, C. L. Perkins, M. Limpinsel, J. C. Hemminger, M. Law, *Adv. Energy Mater.* **2012**, *2*, 1124–1135.
[32] M. Guo, A. Qayum, S. Dong, X. Jiao, D. Chen, T. Wang, *J. Mater. Chem. A* **2020**, *8*, 9239–9247.
[33] Y. Chen, S. Xu, Y. Li, R. J. Jacob, Y. Kuang, B. Liu, Y. Wang, G. Pastel, L. G. Salamanca-Riba, M. R. Zachariah, L. Hu, *Adv. Energy Mater.* **2017**, *7*, 1700482.
[34] J. Cai, X. Han, X. Wang, X. Meng, *Matter* **2020**, *2*, 587–630.
[35] H. G. Kim, H.-B.-R. Lee, *Chem. Mater.* **2017**, *29*, 3809–3826.
[36] Y. Shao, Z. Guo, H. Li, Y. Su, X. Wang, *Angew. Chem. Int. Ed.* **2017**, *56*, 3226–3231; *Angew. Chem.* **2017**, *129*, 3274–3279.
[37] Z. Guo, X. Wang, *Angew. Chem. Int. Ed.* **2018**, *57*, 5898–5902; *Angew. Chem.* **2018**, *130*, 6000–6004.
[38] W. Xiong, Z. Guo, H. Li, R. Zhao, X. Wang, *ACS Energy Lett.* **2017**, *2*, 2778–2785.
[39] Y. Yuan, L. Wang, L. Gao, *Front. Chem.* **2020**, *8*, 1–16.
[40] P. Chiriţă, M. L. Schlegel, *Int. J. Miner. Process.* **2015**, *135*, 57–64.
[41] N. A. Khan, N. Rashid, I. Ahmad, Zahidullah, R. Zairov, H. ur Rehman, M. F. Nazar, U. Jabeen, *Int. J. Hydrogen Energy* **2022**, *47*, 22340–22347.
[42] R. Weerasooriya, M. Makehelwala, A. Bandara, *Colloids Surf. A* **2010**, *367*, 65–69.
[43] P. Chiriţă, M. Descostes, M. L. Schlegel, *J. Colloid Interface Sci.* **2008**, *321*, 84–95.
[44] A. Matamoros-Veloza, O. Cespedes, B. R. G. Johnson, T. M. Stawski, U. Terranova, N. H. de Leeuw, L. G. Benning, *Nat. Commun.* **2018**, *9*, 3125.
[45] G. Panzmer, B. Egert, *Surf. Sci.* **1984**, *144*, 651–664.
[46] M. Mullet, S. Boursiquot, M. Abdelmoula, J.-M. Génin, J.-J. Ehrhardt, *Geochim. Cosmochim. Acta* **2002**, *66*, 829–836.
[47] A. Pratt, I. Muir, H. Nesbitt, *Geochim. Cosmochim. Acta* **1994**, *58*, 827–841.
[48] W. Han, M. Gao, *Cryst. Growth Des.* **2008**, *8*, 1023–1030.
[49] Y. Xu, F. Bahmani, R. Wei, *Microsyst Nanoeng* **2020**, *6*, 75.
[50] G. Li, B. Zhang, F. Yu, A. A. Novakova, M. S. Krivenkov, T. Y. Kiseleva, L. Chang, J. Rao, A. O. Polyakov, G. R. Blake, R. A. de Groot, T. T. M. Palstra, *Chem. Mater.* **2014**, *26*, 5821–5829.
[51] L. M. White, R. Bhartia, G. D. Stucky, I. Kanik, M. J. Russell, *Earth Planet. Sci. Lett.* **2015**, *430*, 105–114.
[52] A. T. Ward, *J. Phys. Chem.* **1968**, *72*, 4133–4139.
[53] M. Motola, M. Čaplovičová, M. Krbal, H. Sopha, G. K. Thirunavukkarasu, M. Gregor, G. Plesch, J. M. Macak, *Electrochim. Acta* **2020**, *331*, 135374.
[54] C. Hu, L. Zhang, J. Gong, *Energy Environ. Sci.* **2019**, *12*, 2620–2645.
[55] H. Valdés, L. M. Molina, J. A. Alonso, *Appl. Surf. Sci.* **2019**, *487*, 244–252.
[56] R. Weber, A. J. Louli, K. P. Plucknett, J. R. Dahn, *J. Electrochem. Soc.* **2019**, *166*, A1779–A1784.
[57] Z. Zhou, L. Wei, Y. Wang, H. E. Karahan, Z. Chen, Y. Lei, X. Chen, S. Zhai, X. Liao, Y. Chen, *J. Mater. Chem. A* **2017**, *5*, 20390–20397.
[58] Y. Liu, J. Wu, K. P. Hackenberg, J. Zhang, Y. M. Wang, Y. Yang, K. Keyshar, J. Gu, T. Ogitsu, R. Vajtai, J. Lou, P. M. Ajayan, B. C. Wood, B. I. Yakobson, *Nat. Energy* **2017**, *2*, 17127.
[59] M. Wang, L. Zhang, M. Huang, Y. Liu, Y. Zhong, J. Pan, Y. Wang, H. Zhu, *Energy Environ. Mater.* **2020**, *3*, 12–18.
[60] A. S. Lim, A. Atrens, *Appl. Phys. A* **1990**, *51*, 411–418.
[61] P. Marcus, I. Olefjord, *Corros. Sci.* **1988**, *28*, 589–602.
[62] M. Sun, Q. Zhang, Q. Chen, X. Hou, W. Peng, Y. Li, F. Zhang, Q. Xia, X. Fan, *Catalysts* **2022**, *12*, 594.
[63] B. Xing, N. Graham, W. Yu, *Commun. Chem.* **2020**, *3*, 38.
[64] T. L. Barr, *J. Phys. Chem.* **1978**, *82*, 1801–1810.
[65] V. Di Castro, S. Ciampi, *Surf. Sci.* **1995**, *331–333*, 294–299.
[66] D. Rickard, G. W. Luther, *Chem. Rev.* **2007**, *107*, 514–562.
[67] A. Anderko, P. J. Shuler, *Comput. Geosci.* **1997**, *23*, 647–658.
[68] S. N. A. Zakaria, N. Hollingsworth, H. U. Islam, A. Roffey, D. Santos-Carballal, A. Roldan, W. Bras, G. Sankar, G. Hogarth, K. B. Holt, N. H. de Leeuw, *ACS Appl. Mater. Interfaces* **2018**, *10*, 32078–32085.
[69] R. Ovcharenko, E. Voloshina, J. Sauer, *Phys. Chem. Chem. Phys.* **2016**, *18*, 25560–25568.
[70] S. Das, H. Sopha, M. Krbal, R. Zazpe, V. Podzemna, J. Prikryl, J. M. Macak, *ChemElectroChem* **2017**, *4*, 495–499.
[71] M. Motola, L. Hromadko, J. Prikryl, H. Sopha, M. Krbal, J. M. Macak, *Electrochim. Acta* **2020**, *352*, 136479.
[72] H. Sopha, Z. Spotz, M. Sepúlveda, M. Alijani, M. Motola, L. Hromadko, J. M. Macak, *Ceram. Int.* **2022**, 1–9. https://doi.org/10.1016/j.ceramint.2022.11.032.
[73] V. C. Anitha, R. Zazpe, M. Krbal, J. Yoo, H. Sopha, J. Prikryl, G. Cha, S. Slang, P. Schmuki, J. M. Macak, *J. Catal.* **2018**, *365*, 86–93.
[74] D. M. Morales, M. Risch, *J. Phys. Energy* **2021**, *3*, 034013.

Manuscript received: January 24, 2023
Revised manuscript received: March 11, 2023
Accepted manuscript online: March 20, 2023
Version of record online: April 27, 2023